2013 IEEE/RSJ International Conference on
Intelligent Robots and Systems (IROS)
November 3-7, 2013. Tokyo, Japan

# On using an Array of Fiber Bragg Grating Sensors for Closed-Loop Control of Flexible Minimally Invasive Surgical Instruments

Roy J. Roesthuis, Sander Janssen and Sarthak Misra

***Abstract*— Flexible minimally invasive surgical instruments can be used to target difficult-to-reach locations within the human body. Accurately steering these instruments requires information about the three-dimensional shape of the instrument. In the current study, we use an array of Fiber Bragg Grating (FBG) sensors to reconstruct the shape of a flexible instrument. FBG sensors have several advantages over existing imaging modalities, which makes them well-suited for use in a clinical environment. An experimental testbed is presented in this study, which includes a tendon-driven manipulator. A nitinol FBG-wire is fabricated, on which an array of twelve FBG sensors are integrated, and distributed over four different sets. This wire is positioned in the backbone of the manipulator. Axial strains are measured using the FBG sensors, from which the curvature of the manipulator is calculated. The three-dimensional manipulator shape is reconstructed from the curvature, which is used to steer the manipulator tip. We are able to steer the manipulator along various trajectories (two-dimensional and three-dimensional), and also reject disturbance loads. We observe a minimum mean tracking error of 0.67 mm for the circular trajectory in closed-loop control. This study demonstrates the potential of steering flexible minimally invasive surgical instruments using an array of FBG sensors.**

## I. Introduction

Recent studies have shown great interest in steering a variety of flexible, minimally invasive surgical (MIS) instruments. These instruments vary from small diameter ($\phi \leq 1$ mm) needles with bevel tips (e.g., for breast biopsies) to flexible catheters (e.g., for beating heart surgery) [1]–[12]. These instruments often have a flexible structure, which causes them to bend when they are subjected to interaction forces. Hence, this allows them to be steered around obstacles, and enables targeting difficult-to-reach locations in the human body. In order to steer such instruments to a desired location, information is required about the shape of the instrument.

Previous research used stereo-vision camera systems to acquire information about the location of the instrument [2]. However, camera-based systems cannot be used *in vivo*. Electromagnetic sensors have also been used to locate the tip of the instrument [10]. Such sensors can be used *in vivo*, but they are sensitive to distortion induced by metallic objects and electrical noise. Hence, this limits the use of electromagnetic localization in a clinical environment. Previous studies used medical imaging techniques, such as ultrasound images, x-ray computed tomography (CT) scans and magnetic resonance imaging (MRI), in order to aquire instrument shape. However, these methods have several drawbacks: Ultrasound has low tissue contrast. MRI has a low refresh rate and hence, is not well-suited for real-time applications. CT exposes the patient to high doses of radiation and hence, is also not recommended for continuous use.

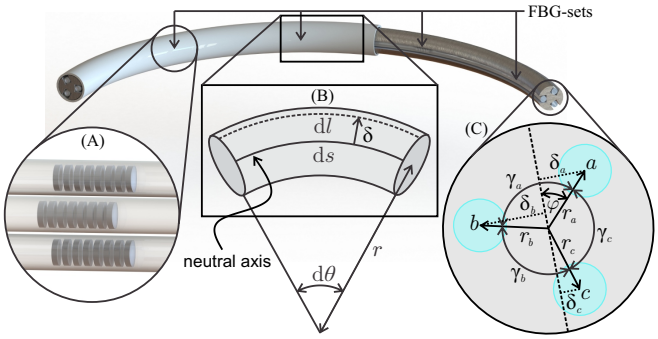


Fig. 1. A section of a flexible instrument (which could be a needle, catheter or colonoscope) is shown. An array of co-located FBG sensors (i.e., FBG-sets) are placed along the instrument shaft. (A) A set of three co-located FBG sensors are used to measure axial strain, which is used to calculate the curvature. (B) Instrument shape is reconstructed from the curvature ($\kappa = 1/r$). (C) A cross-section of the instrument: The position of each fiber is given by the distance from the center of the instrument ($r_a$, $r_b$ and $r_c$) and the angle with respect to the other fibers ($\gamma_a$, $\gamma_b$ and $\gamma_c$). The distance from the fibers to the neutral axis is indicated by $\delta_a$, $\delta_b$ and $\delta_c$.

Fiber Bragg Grating (FBG) sensors can be an alternative to acquire three-dimensional (3D) instrument shape *in vivo*. FBG sensors have several properties which makes them well-suited for biomedical applications, e.g., biocompatibility, non-toxic, chemical inertness and electromagnetical inertness [13]. Also, current technologies enable data acquisition at rates up to 20 kHz with FBG sensors. Hence, this makes them applicable for real-time applications. FBG sensors can be used to measure mechanical strain [14]. Due to the small size of FBG sensors ($\phi \leq 250$ $\mu$m), they can be integrated along the shaft of a flexible MIS instrument (Fig. 1). Integrating an array of FBG sensors along the instrument shaft enables measuring the strain caused by the bending of the instrument. This strain can be used to determine the curvature along the shaft of the instrument at the location of the FBG sensors. This curvature is then used to reconstruct the 3D instrument shape. Previous studies have used FBG sensors to reconstruct the shape of a colonoscope and flexible surgical needles [15]–[19]. These studies have shown that instrument shape can be reconstructed with high accuracy using FBG sensors.

In the current study, we demonstrate using an array of FBG

The authors are affiliated with MIRA – Institute for Biomedical Technology and Technical Medicine, University of Twente, The Netherlands. This research is supported by the Dutch Technology Foundation STW (H-Haptics Project #12159), which is part of the Netherlands Organization for Scientific Research (NWO) and partly funded by the Ministry of Economic Affairs, Agriculture and Innovation.

sensors to steer a flexible instrument. Recently, Abayazid *et al*. demonstrated flexible needle steering using an array of FBG sensors [19]. However, the tip deflections in that study were small (i.e., $\leq$ 5 mm) compared to our study. The goal of our study is to show that FBG sensors have the potential to be used to control a large variety of flexible MIS instruments. In order to demonstrate this, we have constructed a tendon-driven manipulator. This manipulator is actuated by a total of four tendons, allowing it to bend in all directions. A flexible nitinol wire with an array of twelve FGB sensors has been fabricated, and is placed in the hollow backbone of the manipulator. This allows to reconstruct the shape of the manipulator as it deflects. The reconstructed position of the manipulator tip is then used as feedback in a closed-loop control system. The forward and inverse kinematics of the manipulator are derived, and are used in a closed-loop control system to steer the tip of the manipulator to a desired position. The performance of the system is demonstrated in various trajectory tracking experiments. We also evaluate the ability of the system to reject load disturbances.

The paper is organized as follows: Section II describes the methods for reconstructing the 3D shape of a flexible instrument using an array of FBG sensors. In Section III, the kinematics of the robotic manipulator is presented. The experimental setup is presented in Section IV, and the experimental results are discussed in Section V. Finally, we conclude the paper in Section VI, and directions for future work are given.

## II. Three-Dimensional Shape Sensing using Fiber Bragg Grating Sensors

This section describes the methods to reconstruct the 3D shape of a flexible instrument using an array of FBG sensors. First, we describe the method to calculate strain from an FBG sensor. This is followed by the computation of curvature and its direction from a set of FBG sensors. Finally, we describe 3D reconstruction of instrument shape.

### A. Strain Measurement

An FBG has the property to reflect light of a specific wavelength, called the Bragg wavelength ($\lambda_{\mathrm{B}}$), which is given by [14]

$$\lambda_{\mathrm{B}} = 2n_e\Lambda, \tag{1}$$

where $n_e$ is the effective refractive index of the grating in the fiber core and $\Lambda$ is the grating period. The effective refractive index and the grating period are affected by changes in mechanical strain and temperature and hence, this results in a change in the Bragg wavelength. This enables an FBG to be used as a sensor for measuring mechanical strain or temperature. Assuming constant temperature, the shift in Bragg wavelength due to mechanical strain ($\varepsilon_x$) is given by [20]

$$\Delta\lambda_{\mathrm{B}} = \lambda_{\mathrm{B}}\left(1 - p_e\right)\varepsilon_x. \tag{2}$$

The axial strain of an instrument ($\varepsilon_x$) can be measured using FBG sensors. This is done by placing an optical fiber with FBG sensors parallel to the longitudinal axis of the instrument (Fig. 1). Assuming pure bending, the following relationship exists between the axial strain in the fiber and the distance ($\delta$) of the fiber to the neutral bending plane of the instrument [21]:

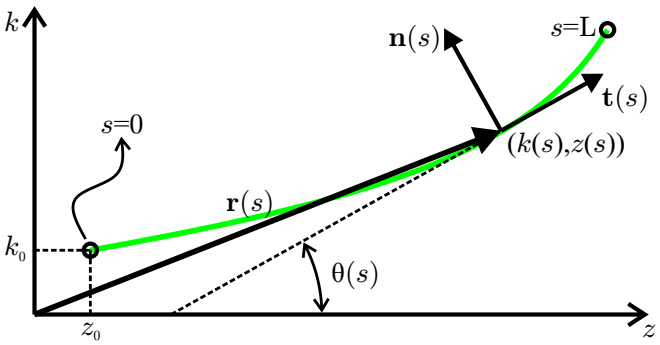


Fig. 2. A planar curve $\left(\mathbf{r}(s)\right)$ is parametrized by the arc length ($s$). The slope of the curve with respect to the $z$-axis is denoted by $\theta(s)$. The Frenet-Serret vectors are also shown: The tangent vector ($\mathbf{t}(s)$) and normal vector ($\mathbf{n}(s)$).

$$\varepsilon_x = \frac{\mathrm{d}s - \mathrm{d}l}{\mathrm{d}l} = -\frac{\delta}{r} = -\kappa\delta, \tag{3}$$

where $\kappa$ and $r$ are the curvature and radius of curvature of the instrument, respectively (Fig. 1). Substituting (3) into (2) gives an expression which relates the shift in Bragg wavelength to curvature

$$\Delta\lambda_{\mathrm{B}} = -\lambda_{\mathrm{B}}\left(1 - p_e\right)\kappa\delta. \tag{4}$$

In the next subsection, we describe the calculation of curvature ($\kappa$) and its direction ($\varphi$) using the strain measurements from a set of multiple co-located FBG sensors.

### B. Curvature Calculation

The curvature and its direction can be determined using strain measurements from a set of multiple FBG sensors at the same location along the instrument shaft (Fig. 1). In theory, two strain mausurements are sufficient to determine the curvature. In practice, temparature changes and axial forces also contribute to the axial strain by an offset ($\varepsilon_0$). Hence, three strain measurements are used to compensate for this offset. The relationship between the axial strain due to bending and the distance from the neutral bending plane is given by (3). Thus, the following set of equations are derived for the strains at the location of three fibers (denoted by $a$, $b$ and $c$) at a cross-section of the needle (Fig. 1):

$$\begin{aligned}
\varepsilon_a &= -\kappa\delta_a + \varepsilon_0 = -\kappa r_a \sin(\varphi) + \varepsilon_0,\\
\varepsilon_b &= -\kappa\delta_b + \varepsilon_0 = -\kappa r_b \sin(\varphi + \gamma_a) + \varepsilon_0,\\
\varepsilon_c &= -\kappa\delta_c + \varepsilon_0 = -\kappa r_c \sin(\varphi + \gamma_a + \gamma_b) + \varepsilon_0,
\end{aligned} \tag{5}$$

where $\varphi$ is the angle between $r_a$ and the neutral axis (Fig. 1), and indicates the direction of the curvature. The position ($r_a$, $r_b$ and $r_c$) and orientation ($\gamma_a$, $\gamma_b$ and $\gamma_c$) of the FBG sensors are assumed to be known and constant (i.e., the neutral plane is always assumed to be at the center of the needle). By solving the set of equations (5), the unknowns are determined (i.e., $\kappa$, $\varphi$ and $\varepsilon_0$). Since the curvature can only be determined at the locations of the FBG sensors,

interpolation needs to be performed to evaluate the curvature along the entire instrument shaft. In the next subsection, we explain the reconstruction of 3D instrument shape using the curvature and its direction.

### C. Three-Dimensional Shape Reconstruction

For this study, we consider the instrument to bend in a single plane, and therefore it can be seen as a planar curve. First, Frenet-Serret frames are used to reconstruct the instrument shape. Next, the direction of curvature ($\varphi$) is used to calculate the position of the planar curve in 3D space.

Let $\mathbf{r}(s)$ be a planar curve (Fig. 2) parametrized by the arc length ($s$)

$$\mathbf{r}(s) = \begin{bmatrix} z(s) \\ k(s) \end{bmatrix}. \tag{6}$$

The curvature of this planar curve is given by

$$\kappa(s) = \frac{\mathrm{d}\theta(s)}{\mathrm{d}s}, \tag{7}$$

where $\theta(s)$ is the angle between the tangent at a point along the curve and the positive direction of the $z$-axis (i.e., slope of the curve). Using Frenet-Serret frames, the tangent vector of this curve is defined as

$$\begin{aligned} \mathbf{t}(s) = \frac{\mathrm{d}\mathbf{r}(s)}{\mathrm{d}s} &= \begin{bmatrix} \frac{\mathrm{d}z(s)}{\mathrm{d}s} & \frac{\mathrm{d}k(s)}{\mathrm{d}s} \end{bmatrix}^{\mathrm{T}} \\ &= \begin{bmatrix} \cos(\theta(s)) & \sin(\theta(s)) \end{bmatrix}^{\mathrm{T}}. \end{aligned} \tag{8}$$

Since the curvature is known from the FBG sensor measurements, the slope of the curve $\big(\theta(s)\big)$ is calculated by integrating the curvature (7)

$$\theta(s) = \int_0^s \kappa(s)\,\mathrm{d}s + \theta_0, \tag{9}$$

where $\theta_0$ is the intial slope (i.e., $s = 0$). The curve $(\mathbf{r}(s))$ can then be calculated by integrating the tangent vector in (8)

$$\begin{aligned} \mathbf{r}(s) = \begin{bmatrix} z(s) \\ k(s) \end{bmatrix} &= \int_0^s \mathbf{t}(s)\,\mathrm{d}s \\ &= \begin{bmatrix} \int_0^s \cos(\theta(s))\,\mathrm{d}s + z_0 \\ \int_0^s \sin(\theta(s))\,\mathrm{d}s + k_0 \end{bmatrix}, \end{aligned} \tag{10}$$

where $z_0$ and $k_0$ are the initial deflections. The direction of the curvature ($\varphi$) and deflection $k(s)$ are used to calculate the $x$-position and $y$-position of the curve

$$\begin{aligned} x(s) &= k(s)\cos(\varphi), \\ y(s) &= k(s)\sin(\varphi). \end{aligned} \tag{11}$$

Thus, the 3D position of a point along the shaft of the instrument $\Big(\mathbf{r}(s) = \big[x(s),\, y(s),\, z(s)\big]^{\mathrm{T}}\Big)$ can be calculated using the curvature and its direction.

## III. Kinematics of the Manipulator

This section describes the kinematics (forward and inverse) of the manipulator that will be used for closed-loop experiments with the FBG sensors (Fig. 3). The manipulator consists of a flexible backbone (of length $l_b$) on which a series of equally spaced tendon guides are mounted. Four

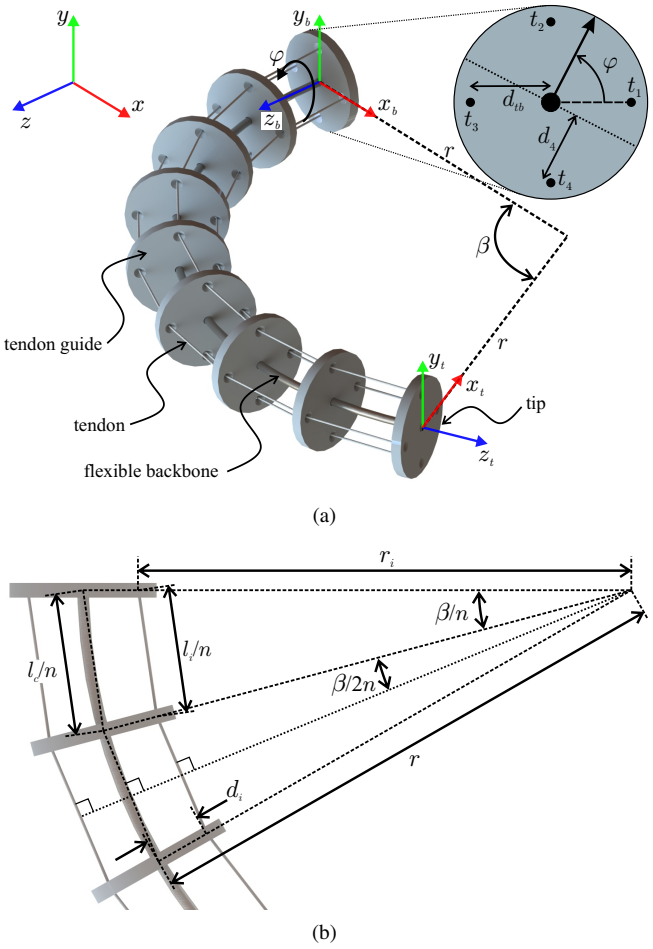


Fig. 3. (a) The manipulator consists of a flexible backbone on which tendon guides are mounted. Actuating a total of four tendons $(t_1, \ldots, t_4)$ causes the manipulator to deflect with a constant radius of curvature ($r$) and out-of-plane bending angle ($\varphi$). In this figure, the manipulator bends in the $xz$-plane (i.e., $\varphi = 0$). (b) Top view of a section of the continuum manipulator in a bent configuration. The manipulator is divided into $n$ segments, where each segment is defined between two subsequent tendon guides.

tendons are routed through these guides at 90° angles from one another. The tendons are all connected to the tendon guide at the tip. The manipulator deflects in a single-bend shape when the tendons are actuated (i.e., pulled).

### A. Forward Kinematics

We determine the forward kinematics of the manipulator to derive the relationship between the tendon lengths $(l_1, \ldots, l_4)$ and the position of the manipulator tip ($x_t$, $y_t$, $z_t$). The forward kinematics of such a continuum-style manipulator has been described by Jones and Walker for a three-tendon driven manipulator [22]. Further, Webster and Jones presented a simplified derivation of these kinematics [6] both for the case of three actuators and four actuators. Their approach assumes that the manipulator bends with a constant radius of curvature ($r$). We use the same approach to derive the kinematics of our four-tendon driven manipulator (Fig. 3a). The position of the manipulator tip is determined by the radius of curvature ($r$), and the out-of-plane bending angle ($\varphi$). Note that this angle is equal to the direction of the curvature (Section II-B), in case the first tendon ($t_1$) is aligned with

fiber $a$.

The length of a hypothetical center cable (Fig. 3b) is given by

$$l_c = 2nr \sin\left(\beta/2n\right), \tag{12}$$

where $n$ indicates the number of segments and $\beta$ is equal to $l_b/r$. Further, the lengths of the individual tendons ($l_i$, for $i = 1 \dots 4$) are given by

$$l_i = 2nr_i \sin\left(\beta/2n\right), \tag{13}$$

The radius of curvature ($r_i$) at for each tendon is related to the distance of the tendon to the neutral axis ($d_i$) by

$$r_i = r - d_i, \tag{14}$$

where $d_i$ is related to the out-of-plane bending angle by

$$d_i = d_{tb} \cos\left(\varphi + (i-1)\pi/2\right), \tag{15}$$

where $d_{tb}$ is the distance from the tendon to the backbone (Fig. 3a). Substituting (15) into (13), and combining with (12) gives

$$l_c = l_i + 2nd_{tb} \cos\left(\varphi + (i-1)\pi/2\right) \sin\left(\beta/2n\right). \tag{16}$$

Combining (16) for all four tendons, results in the following:

$$l_c = \frac{l_1 + l_2 + l_3 + l_4}{4}. \tag{17}$$

As was shown by Webster and Jones, the out-of-plane bending angle is determined by [6]

$$\varphi = \tan^{-1}\left(\frac{l_4 - l_2}{l_3 - l_1}\right). \tag{18}$$

Applying trigonmetric relation to a section of the manipulator (Fig. 3b), the following relationship can be derived for the radius of curvature:

$$r = r_i \frac{l_c/n}{l_i/n} = (r - d_i)\frac{l_c/n}{l_i/n} = d_i \frac{l_c}{l_c - l_i}. \tag{19}$$

Substituting (15) for $d_i$ (for $i = 1$), and (17) for $l_c$ into (19) gives the radius of curvature as a function of the tendon lengths. After simplifying, the result is given as:

$$r = \frac{d_{tb}\left(l_1 + l_2 + l_3 + l_4\right)\left(l_1 - l_3\right)}{\left(l_2 - 3l_1 + l_3 + l_4\right)\sqrt{\left(l_2 - l_4\right)^2 + \left(l_1 - l_3\right)^2}}. \tag{20}$$

The position of the tip of the manipulator is now completely described by the out-of-plane bending angle (18), and radius of curvature (20). In the next subsection, the inverse kinematics are derived which are required for controlling the manipulator.

### B. Inverse Kinematics

In order to steer the tip towards a desired position $\left(\mathbf{p}_\mathrm{d} = \begin{bmatrix} x_\mathrm{d} & y_\mathrm{d} & z_\mathrm{d} \end{bmatrix}^\mathrm{T}\right)$, the inverse kinematics of the manipulator needs to be derived. These provide the inputs of the system (i.e., tendon lengths) as a function of the tip position. Given the desired position of the manipulator tip, the out-of-plane bending angle is calculated by

$$\varphi = \tan^{-1}\left(\frac{y_\mathrm{d}}{x_\mathrm{d}}\right) \tag{21}$$

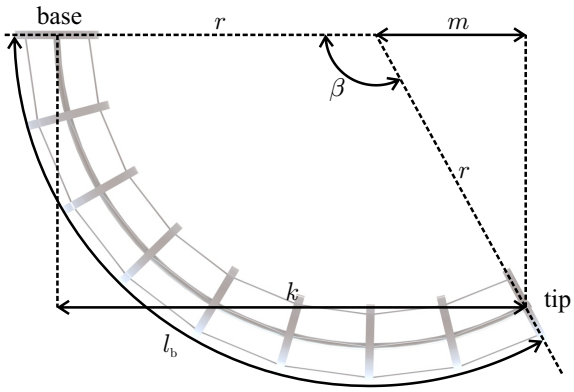


Fig. 4. Top view of the manipulator (with length $l_b$) as it bends with a constant radius of curvature ($r$). The angle $\beta$ is related to the radius of curvature by: $\beta = l_b/r$. The deflection of the tip with respect to the base is given by $k$.

The required radius of curvature is then given by (Fig. 4)

$$r = k + m, \tag{22}$$

where $k$ and $m$ are

$$k = \sqrt{({x_\mathrm{d}}^2 + {y_\mathrm{d}}^2)}, \tag{23}$$

and

$$m = r\cos\left(\beta\right) = r\cos\left(\frac{l_\mathrm{b}}{r}\right). \tag{24}$$

Substituting (23) and (24) into (22) provides us with the following expression:

$$r = \sqrt{({x_\mathrm{d}}^2 + {y_\mathrm{d}}^2)} + r\cos\left(\frac{l_\mathrm{b}}{r}\right). \tag{25}$$

We solve (25) numerically to determine the radius of curvature ($r$). Knowing the required radius of curvature and substituting the out-of-plane bending angle from (21) into (15), we can calculate the individual tendon lengths using (13).

## IV. Experimental Testbed

This section describes the setup which is used as a testbed for experiments with the manipulator. We also present the controller which is used to steer the manipulator tip.

### A. Setup

A setup (Fig. 5) is fabricated to actuate the four tendons and allows insertion of the manipulator, whose kinematics are presented in Section III. The manipulator is connected to a carriage which is mounted onto a linear stage. The carriage holds four motors which enables independent actuation of the tendons. The linear stage allows translation of the manipulator along the insertion axis ($z$-axis).

The backbone of the manipulator consists of a nitinol tube ($\phi_{outer}$ 1.6 mm and $\phi_{inner}$ 1.2 mm) with a length of 160 mm. The tendon guides are circular polymer disks ($\phi$ 20 mm), and these are glued onto the backbone. The tendons are made from fishing wire ($\phi$ 0.40 mm), and are routed through the tendon guides at a distance of 7.5 mm from the center of the backbone ($d_{tb}$ = 7.5 mm). A total of eight tendon guides are glued onto the backbone, spaced 20 mm apart. This spacing is chosen such that the ratio

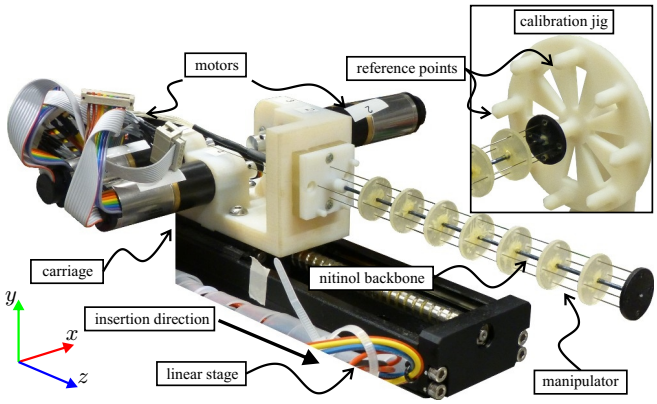


(a)

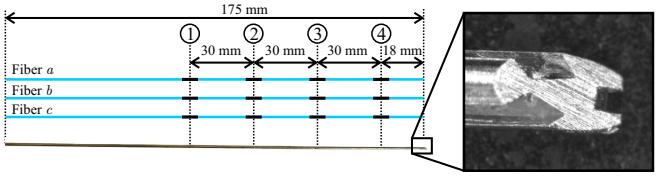


(b)

Fig. 5. (a) The experimental setup consists of a linear stage which enables translation of the manipulator in the insertion direction (i.e., $z$-axis). A carriage is mounted on the linear stage, and holds the four motors to actuate the four tendons. The manipulator itself is also mounted onto this carriage. The top right picture shows the jig which is used to calibrate the Fiber Bragg Grating (FBG) sensors. (b) The nitinol wire ($\phi$ 1.0 mm) with the array of twelve FBG sensors, distributed over four sets ($\text{FBG}_1, \ldots, \text{FBG}_4$). The inset shows the grooves at the tip of the wire in which the fibers are integrated.

between tendon offset ($d_{tb}$) and spacing of cable supports is near the optimal ratio of 0.4 [23]. A nitinol wire ($\phi$ 1.0 mm) with an integrated array of FBG sensors is used to sense the shape of the manipulator (Fig. 5b). This wire is inserted into the hollow backbone of the manipulator. Additional details about the fabrication of this FBG wire are presented in Roesthuis *et al.* [18].

### B. Controller Implementation

The system architecture of the experimental testbed is shown in Fig. 6. The tip of the manipulator is controlled along each axis using a Proportional-Integral-Derivative (PID-) controller. The error between the desired tip position and the reconstructed tip position using FBG sensors is used as input for the PID-controller. The output of the PID-controller is a modified tip position. Using the inverse kinematics of the manipulator (Section III-B), the corresponding tendon lengths are determined.

The manipulator is controlled at a rate of 100 Hz. The strain information is read from the FBG sensors using a Deminsys Python Interrogator (Technobis Mechatronics, Uitgeest, The Netherlands). This interrogator communicates with a desktop computer using the UDP-protocol. A multithreaded C++-program is written which reads the UDP-packets and calculates the appropriate control outputs. This program also communicates with Elmo motor controllers (Elmo Motion Control Ltd., Petach-Tikva, Israel) which drive the motors to the desired position.

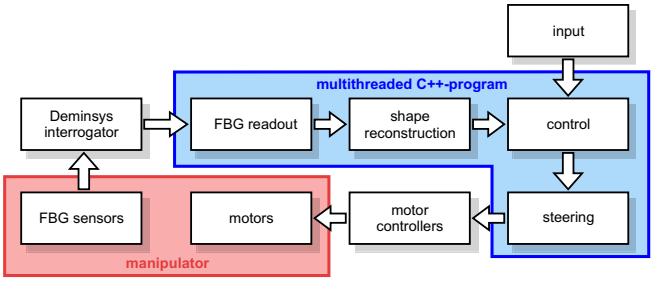


Fig. 6. The system architecture of the experimental testbed. The Fiber Bragg Grating (FBG) sensors produce a change in Bragg wavelength as they are subjected to strain. This change in wavelength is transferred through the Deminsys interrogator to the C++-program, and is then converted to strains. The shape reconstruction algorithm calculates tip position from these strains. The output of the control depends on the error between the desired tip position provided by the input, and the reconstructed tip position. The steering algorithm calculates motor positions from the controller output, and the manipulator is actuated accordingly.

## V. Experimental Results

This section describes the results of the various experimental studies conducted with our testbed. First, the FBG sensors are calibrated and the gains of the PID-controller are tuned. Next, experiments are performed to evaluate the trajectory tracking performance of the system. Finally, the ability of the system to reject disturbance loads are also evaluated.

### A. Setup Calibration

The positions and orientations of the FBG sensors along the shaft of the FBG wire are assumed to be known. However, there are uncertainties during the fabrication of the FBG sensors and therefore, calibration of the FBG sensors are required. A calibration jig is made which consists of a number of reference points which are distributed along a circle ($\phi$ 60 mm), as shown in Fig. 5. The FBG sensors are calibrated by manually positioning the manipulator tip at the reference points ($x_{\text{ref}}, y_{\text{ref}}$), and then reconstructing the tip position. The reconstructed tip positions ($x_t, y_t$) are scaled both along the $x$-axis and $y$-axis such that the error between the reconstruction and the reference point is minimized. Scaling factors of 0.89 and 0.87 along the $x$-axis and $y$-axis are determined to give minimum errors. The errors before and after the calibration procedure are provided in Table I. The gains of the PID-controller are tuned by observing the step-response of the system. The following gains result in a

TABLE I

The mean errors and standard deviation (in brackets) are provided before and after calibration of the Fiber Bragg Grating (FBG) sensors. The manipulator tip is directed towards each reference position ($x_{\text{REF}}, y_{\text{REF}}$) in mm. Each experiment is repeated three times.

| | Before calibration (mm) | | After calibration (mm) | |
|---|---|---|---|---|
| ($x_{\text{ref}}, y_{\text{ref}}$) | $x$ | $y$ | $x$ | $y$ |
| (30, 0) | 1.97 (0.57) | 0.48 (0.20) | 1.06 (0.52) | 0.42 (0.17) |
| (0, 30) | 0.57 (0.49) | 4.24 (0.35) | 0.52 (0.44) | 0.54 (0.31) |
| (-30, 0) | 4.42 (0.53) | 0.32 (0.28) | 1.15 (0.48) | 0.29 (0.25) |
| (0, -30) | 1.21 (0.28) | 3.06 (0.41) | 1.09 (0.26) | 0.51 (0.37) |
| Mean | 2.04 (1.58) | 2.03 (1.77) | 0.96 (0.46) | 0.44 (0.26) |

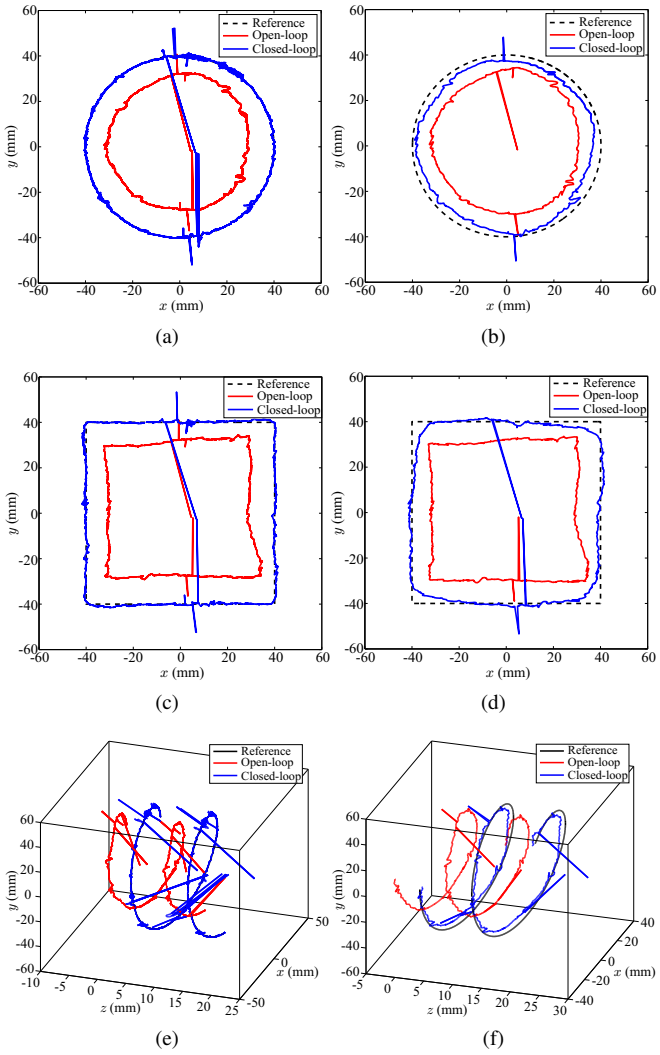


Fig. 7. Trajectory tracking with manipulator tip for a circle (2D), a square (2D) and a helix (3D). Open-loop results (red) are compared with closed-loop results (blue). (a) Circle (40 mm radius), speed is 2 deg/s. (b) Circle (40 mm radius), speed is 30 deg/s. (c) Square (80 mm edges), speed is 5 mm/s. (d) Square (80 mm edges), speed is 20 mm/s. (e) Helix, (40 mm radius), speed is 2 deg/s. (f) Helix, (40 mm radius), speed is 30 deg/s. ***Please refer to the attached video that demonstrates the results of the trajectory tracking experiments using our testbed.***

fast reponse with little overshoot ($\leq$1%): $K_p$ = 2.2, $K_i$ = 1.0 and $K_d$ = 0.2. These gains are used in all of the following experiments in this study.

### B. Trajectory Tracking

The trajectory tracking performance of the system is evaluated by controlling the tip of the manipulator for three different cases; tracking a circle (two-dimensional (2D)), a square (2D) and a helix (3D). The circle has a radius of 40 mm and is evaluated at a slow speed (2 deg/s) and a high speed (30 deg/s). The square has edges of 80 mm, and is also evaluated at a slow speed (5 mm/s) and a high speed (20 mm/s). The helix has a radius of 40 mm and a pitch of 10 mm, and is evaluated at a slow speed (2 deg/s) and a high speed (30 deg/s). The experiments are done both in open-loop and closed-loop control. The reference and

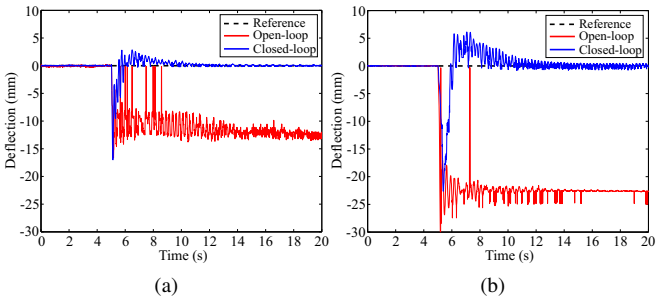


Fig. 8. The response of the system to a load disturbance for open-loop control and closed-loop control. A weight is added to the tip of the manipulator at 5 s. (a) 20 g. weight. (b) 50 g. weight. ***Please refer to the attached video that demonstrates the results of the load disturbance experiments using our testbed.***

experimental trajectories are shown in Fig 7. The resulting tracking errors are provided in Table II. The mean errors become significantly smaller for closed-loop control. Large errors occur near the corners of the square due to change of direction when the speed is increased.

It can be seen that in all the experiments the system suffers from systematic errors which could be attributed to the mechanical system. The holes through which the tendons are routed are not smooth, and this results in a erratic behaviour of the manipulator tip in some parts of the trajectory. The larger spikes are the result of systematic errors in the measurement of the tip position. The cause for these measurement errors is currently unknown and requires further investigation.

### C. Load Disturbance Rejection

The ability of the system to reject load disturbances is evaluated for two experimental cases. The manipulator is commanded to a straight orientation (i.e., $x_d = y_d = 0$). In the first case a weight of 20 g. is placed at the manipulator tip, and in the second case of weight of 50 g. is used. The resulting response of the system is evaluated both for open-loop control and closed-loop control (Fig. 8). It can be seen that in both cases the system quickly ($\leq 7s$.) reacts to the load disturbance, and is able to maintain the desired position without becoming unstable.

## VI. Conclusions and Future Work

In this study, we demonstrated using an array of FBG sensors for the closed-loop control of a flexible manipulator. An experimental testbed is presented, which consists of a flexible, four tendon-driven manipulator. A total of twelve sensors, distributed over four different sets are embedded on a flexible nitinol wire. This wire is introduced into the hollow backbone of the manipulator. Strain measurements from the FBG sensors are used to reconstruct 3D manipulator shape. The reconstructed tip position is used as feedback in a PID-controller to steer the tip of the manipulator to a desired position.

### A. Conclusions

The performance of the system is demonstrated for three trajectory-tracking cases, evaluated at a slow speed and a

TABLE II

COMPARISON BETWEEN THE TRAJECTORY TRACKING ERRORS (IN MM) FOR OPEN-LOOP CONTROL AND CLOSED-LOOP CONTROL. THE MEAN ERROR AND THE STANDARD DEVIATION (IN BRACKETS) ARE GIVEN.

| Case | Open-loop | Closed-loop |
|---|---|---|
| Circle (2 deg/s) | 10.47 (1.82) | 0.67 (1.13) |
| Circle (30 deg/s) | 8.79 (1.73) | 2.96 (0.83) |
| Square (5 mm/s) | 11.70 (1.91) | 1.17 (1.02) |
| Square (20 mm/s) | 10.38 (1.52) | 2.48 (1.92) |
| Helix (2 deg/s) | 14.00 (3.39) | 0.87 (1.88) |
| Helix (30 deg/s) | 11.67 (3.15) | 3.93 (1.50) |

high speed: circle (2D), a square (2D) and a helix (3D). The trajectory tracking performance is shown to be greatly improved when closed-loop control is applied. The mean trajectory tracking errors for the open-loop at slow speeds are; 10.47 mm for the circle, 11.70 mm for the square and 14.00 mm for the helix. Closed-loop control shows significant performance increase. The mean trajectory tracking errors are: 0.67 mm for the circle, 1.17 mm for the square and 0.87 mm for the helix. Finally, the ability of the system to reject disturbance loads is demonstrated for two experimental cases: 20 g. and 50 g. weights are hung at the tip. The system is able to maintain the tip at the desired location despite the added load. The results of this study show that FBG sensors can be integrated on a flexible instrument, and used for closed-loop control of the instrument.

### *B. Future Work*

In the current work, we demonstrated closed-loop control using an array of FBG sensors on a manipulator with a single bending segment. As part of future studies, we will investigate shape sensing (using FBG sensors) for instruments with multiple bending segments. The current manipulator did not suffer from non-linear effects such as backlash or hysteresis. Hence, we were able to succesfully control the manipulator using a simple (linear) PID-controller. In practice, surgical instruments often suffer from non-linear effects. A PID-controller will not suffice in those cases, and we will investigate using a non-linear control method in order to steer more clinically relevant instruments. While we aim to continue to improve our controller architecture, our current study demonstrates the feasibility and potential of reconstructing the shape of flexible MIS instruments, and steering them for a variety of clinical applications.

## REFERENCES


[1] N. Abolhassani, R. V. Patel, and M. Moallem, "Needle insertion into soft tissue: A survey," *Medical Engineering and Physics*, vol. 29, no. 4, pp. 413–431, 2007.

[2] D. B. Camarillo, C. R. Carlson, and J. K. Salisbury, "Task-space control of continuum manipulators with coupled tendon drive," in *The International Symposium on Experimental Robotics (ISER)* (O. Khatib, V. Kumar, and G. J. Pappas, eds.), vol. 54 of *Springer Tracts in Advanced Robotics*, pp. 271–280, Athens, Greece, Springer, July 2008.

[3] D. Trivedi, C. D. Rahn, W. M. Kier, and I. D. Walker, "Soft robotics: Biological inspiration, state of the art, and future research," *Journal of Applied Bionics and Biomechanics*, vol. 5, pp. 99–117, September 2008.

[4] J. Ding, K. Xu, R. Goldman, P. Allen, D. Fowler, and N. Simaan, "Design, simulation and evaluation of kinematic alternatives for insertable robotic effectors platforms in single port access surgery," in *Proceedings of the IEEE International Conference on Robotics and Automation (ICRA)*, pp. 1053–1058, Anchorage, USA, May 2010.

[5] P. Dupont, J. Lock, B. Itkowitz, and E. Butler, "Design and control of concentric-tube robots," *IEEE Transactions on Robotics*, vol. 26, pp. 209–225, April 2010.

[6] R. J. Webster and B. A. Jones, "Design and kinematic modeling of constant curvature continuum robots: A review," *The International Journal of Robotics Research*, vol. 29, no. 13, pp. 1661–1683, 2010.

[7] B. Bardou, P. Zanne, F. Nageotte, and M. De Mathelin, "Control of a multiple sections flexible endoscopic system," in *Proceedings IEEE International Conference of Intelligent Robots and Systems (IROS)*, pp. 2345–2350, Taipei, Taiwan, October 2010.

[8] A. Bajo, R. E. Goldman, and N. Simaan, "Configuration and joint feedback for enhanced performance of multi-segment continuum robots," in *Proceedings of the IEEE International Conference on Robotics and Automation (ICRA)*, pp. 2905–2912, Shanghai, China, May 2011.

[9] S. B. Kesner and R. D. Howe, "Position control of motion compensation cardiac catheters," *IEEE Transactions on Robotics*, vol. 27, no. 6, pp. 1045–1055, 2011.

[10] R. S. Penning, J. Jung, N. J. Ferrier, and M. R. Zinn, "An evaluation of closed-loop control options for continuum manipulators," in *Proceedings of the IEEE International Conference on Robotics and Automation (ICRA)*, pp. 5392–5397, St. Paul, Minnesota, USA, May 2012.

[11] A. Reiter, A. Bajo, K. Iliopoulos, N. Simaan, and P. K. Allen, "Learning-based configuration estimation of a multi-segment continuum robot," in *Proceedings of the IEEE/EMBS International Conference in Biomedical Robotics and Biomechatronics (BioRob)*, pp. 829–834, Rome, Italy, June 2012.

[12] E. Butler, R. Hammond-Oakley, S. Chawarski, A. Gosline, P. Codd, T. Anor, J. Madsen, P. Dupont, and J. Lock, "Robotic neuroendoscope with concentric tube augmentation," in *Proceedings IEEE International Conference of Intelligent Robots and Systems (IROS)*, pp. 2941–2946, Vilamoura, Portugal, October 2012.

[13] V. Mishra, N. Singh, U. Tiwari, and P. Kapur, "Fiber grating sensors in medicine: Current and emerging applications," *Sensors and Actuators A: Physical*, vol. 167, no. 2, pp. 279–290, 2011.

[14] A. Othonos, K. Kalli, D. Pureaur, and A. Mugnier, *Optical Sciences*, ch. Fibre Bragg Gratings, pp. 189–262. Springer, 2006.

[15] X. Yi, J. Qian, L. Shen, Y. Zhang, and Z. Zhang, "An innovative 3d colonoscope shape sensing sensor based on fbg sensor array," in *Proceedings of the IEEE International Conference on Information Acquisition (ICIA)*, pp. 227–232, Jefu Island, Republic of Korea, July 2007.

[16] Y. L. Park, S. Elayaperumal, B. Daniel, S. C. Ryu, M. Shin, J. Savall, R. Black, B. Moslehi, and M. Cutkosky, "Real-time estimation of 3-d needle shape and deflection for mri-guided interventions," *IEEE/ASME Transactions on Mechatronics*, vol. 15, no. 6, pp. 906–915, 2010.

[17] K. Henken, D. van Gerwen, J. Dankelman, and J. J. van den Dobbelsteen, "Accuracy of needle position measurements using fiber bragg gratings," *Minimally Invasive Therapy & Allied Technologies*, vol. 21, no. 6, pp. 408–414, 2012.

[18] R. J. Roesthuis, M. Kemp, J. J. van den Dobbelsteen, and S. Misra, "Three-dimensional needle shape reconstruction using an array of fiber bragg grating sensors," *IEEE/ASME Transactions on Mechatronics*, 2013. *In Press*, doi: 10.1109/TMECH.2013.2269836.

[19] M. Abayazid, M. Kemp, and S. Misra, "3d flexible needle steering in soft-tissue phantoms using fiber bragg grating sensors," in *Proceedings of the IEEE International Conference on Robotics and Automation (ICRA)*, pp. 5507–5512, Karlsruhe, Germany, May 2013.

[20] O. Hill and G. Meltz, "Fiber bragg grating technology fundamentals and overview," *Journal of Lightwave Technology*, vol. 15, pp. 1263–1276, August 1997.

[21] J. Gere and S. Timoshenko, *Mechanics of Materials*. Stanley Thornes, 1999.

[22] B. Jones and I. Walker, "Kinematics for multisection continuum robots," *IEEE Transactions on Robotics*, vol. 22, pp. 43–55, February 2006.

[23] C. Li and C. D. Rahn, "Design of continuous backbone, cable-driven robots," *Journal of Mechanical Design*, vol. 124, no. 2, pp. 265–271, 2002.